ACS OMEGA

Open Access

http://pubs.acs.org/journal/acsodf

Article

Optimized Design of Solid−Liquid Dual-Impeller Mixing Systems for Enhanced Efficiency

Ding Xia, Zijian Mao, Shuiqing Zhou,* Xing He, and Yixi Wang

Cite This: *ACS Omega* 2023, 8, 47635−47645

Read Online

ACCESS | Metrics & More | Article Recommendations | Supporting Information

ABSTRACT: Flow interferences occur in the dual-impeller stirred tank between paddles as well as between paddles and baffles and the tank wall, leading to inefficient utilization of the stirring energy. To address this issue, this study investigates the flow characteristics within the mixing tank using Euler−Euler numerical simulation and the particle image velocimetry (PIV) experimental method. The three-dimensional nonconstant flow characteristics are analyzed to optimize the critical stirrer geometry. By employing the Sobol method, an approximate model is established for sensitivity analysis to identify key parameters affecting the solid−liquid dual-impeller stirred tank's performance. Numerical simulations demonstrate that the optimized stirred tank exhibits a significantly improved solid−liquid suspension capacity and considerably reduces flow losses near the wall and baffle areas. Under the designated conditions, the cloud height is increased by 8.7%, and power consumption is reduced by 15.6% compared to the prototype. PIV tests performed on the stirred tank before and after optimization confirmed the reliability of the obtained optimization results. The primary objective of this study is to enhance mixing efficiency and homogeneity in solid−liquid mixing tanks while concurrently minimizing energy consumption and cost. These results validate the feasibility of employing a multiobjective optimal design approach that combines the RBF agent model with the Sobol method. The findings offer valuable insights for the design of similar mixing tanks.

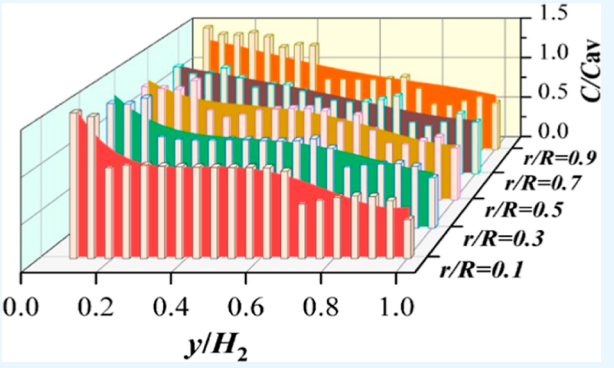

1. INTRODUCTION

The stirred reactor is widely used in the chemical, fermentation, and pharmaceutical industries due to its flexibility of operation and mixing efficiency.[1,2] In recent decades, there has been a trend toward larger and more integrated stirred tanks for various applications, and multilayer impellers are widely used for their higher mixing efficiency.[3,4] In multi-impeller mixing systems, the operating parameters and geometric configuration of the mixing tank can dramatically affect the hydraulic performance, mixing performance, and energy consumption,[5] while the traditional standard design is difficult to meet the requirements of progressively increasing applications. In the chemical industry, green and energy-efficient stirred reaction tank design with efficient mixing performance has been the goal pursued by researchers, and design optimization studies of stirred tanks are necessary to achieve economic and efficient production.[6]

A multi-impeller stirred reaction tank is complex and variable, with solid−liquid, gas−liquid, and gas−liquid−solid multiphase systems, in which solid−liquid two-phase flow is one of the most widely used multiphase systems; its research has been relatively mature.[7,8] For most solid−liquid mixing vessels, the level of suspension and homogeneity of the solid phase are important to researchers. Martina et al.[9] employed a conductivity probe to examine solid concentration profiles at various heights and radii within the vessel. Their study aimed to analyze the distribution of the solid mass and the suspension of solid particles with varying velocities. Li et al.[10] conducted particle image velocimetry (PIV) experiments and found that the particles are only partially suspended before reaching the critical suspension speed, and the rest of the particles will accumulate at the bottom, obstructing the flow near the tank bottom. Blais et al.[11] and Hosseini et al.[12] investigated the liquid kinetic characteristics and solid motion and distribution characteristics of two-phase fluids under different operating conditions using Euler−Lagrange and Euler−Euler methods, respectively.

Different types of impellers, such as pitched blade turbine (PBT),[13] twisted blade turbine (TBT),[14] and curved blade turbine[15] are widely used in mixing and blending systems, but poor mixing areas such as the bottom deposition zone, wall low-speed zone, and baffle dissipation zone still exist during

Received: August 6, 2023
Revised: November 3, 2023
Accepted: November 22, 2023
Published: December 7, 2023

use. For a better discrete-phase suspension effect and mixing uniformity, it is often necessary to continuously increase the stirring speed, but this implies higher power consumption.[16] Consequently, the stirring geometry needs to be further optimized to improve the mixing effect. Steiros et al.[17] investigated the correlation between the vortex coherence and turbulent kinetic energy of various impellers, including thickened blades, perforated blades, and fractal blades. Chen et al.[18] designed a new long and short blade (LSB) impeller and the proposed LSB impeller was found to be more effective in terms of solid particles. Zhang et al.[19] designed a serrated trailing edge blade based on the bionic principle, which enhances the solid−liquid mixing efficiency and reduces the power consumption compared to the PBT. However, the existing optimization design studies often focus on a single mixing geometry; there are fewer studies on the overall optimization of the mixing system, and the summarized laws are usually more limited and difficult to apply. However, the existing optimization design studies often focus on an individual mixing geometry,[20,21] and there are fewer studies on the overall optimization of the mixing system, and the summarized laws usually have greater limitations and are difficult to apply.

In the realm of industrial equipment modeling and optimization, achieving precision and practicality in outcomes remains a paramount concern. To address this, scholars have embraced innovative methods, such as the integration of adaptive mixing techniques, alternative models, and computational fluid dynamics (CFD) with multiobjective intelligent optimization approaches.[22,23] This integration not only aims to reduce computational requirements by minimizing CFD simulations but also reinvigorates stirred reactor optimization studies, especially for the most widely used dual impeller systems.[24] This study delves into the intricate task of enhancing solid−liquid mixing uniformity while simultaneously minimizing power consumption in dual-impeller mixing tanks, which is of great significance in industrial applications. We introduce a sensitivity analysis-driven design approach, utilizing the Euler−Euler method and the Sobol method for RBF approximation model construction, to investigate key variables influencing overall mixing system performance. Our objectives encompass the optimization of dual-impeller tank design, spanning geometry and operational parameters through multiobjective optimization. Key objectives include enhancing the solid−liquid mixing uniformity and reducing power consumption. The results demonstrate a dual-impeller mixing system aligned with optimization objectives with rigorous validation performed via PIV testing. This study not only elucidates the precise application of the Sobol method but also underscores its pivotal role in optimizing dual-impeller mixing tanks for enhanced industrial applications.

2. METHODOLOGY

2.1. Experimental Methodology. The use of a single impeller becomes impractical in mixing tanks with a high height-to-diameter ratio. In solid−liquid mixing systems, axial impellers are very important for the mixing effect, especially to improve the suspension of particles at the bottom and reduce sedimentation. In multi-impeller systems, radial flow is also critical. The object to be optimized in this paper is the immobilized enzyme reaction tank with a dual-impeller system, as shown in Figure 1, whose main flow field structures are tank body, tank bottom, baffle, and stirrer (including stirring shaft,

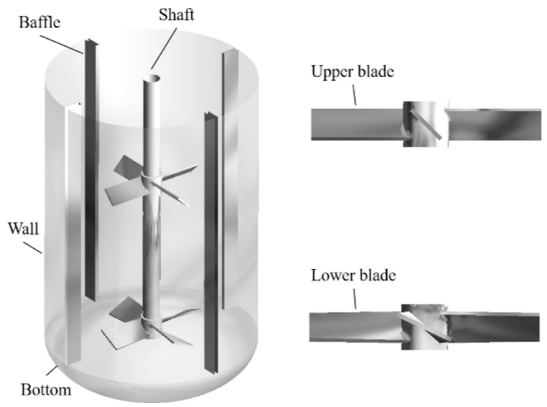

Figure 1. Structure of the dual-impeller mixing tank.

upper impeller, and lower impeller). Among them, the tank bottom is a standard elliptical head, the upper layer is a four-blade PBT, which is a typical mixed flow impeller, and the lower layer is a four-blade TBT, which is an axial impeller with a better effect. Both impellers operate in a down-pumping mode. In the prototype impeller, the upper impeller bevel angle is 45°, the lower impeller outer edge bevel angle is 25°, and the lower impeller inner edge bevel angle is 45°.

With the development of experimental measurement techniques, PIV is widely used in hydrodynamic measurements as a noncontact-type measurement technique capable of providing rich fluid flow information (e.g., velocity field and turbulent kinetic energy field) for stirred reactors. In this study, a 2D PIV system was used. The 2D PIV system (Microvec Pte Ltd., Beijing, China) adopted in the present work consisted of a dual Vlite series 532 nm dual pulse laser (Beamtech Optronics Co., Ltd., 500 mJ, 10 Hz, Beijing, China), a high-resolution CCD camera with 6600 × 4400 pixels, a synchronizer, and the commercial software MicroVec-V3.6.[19]

The test principle is shown in Figure 2a and the experimental setup is shown in Figure 2b. To ensure a

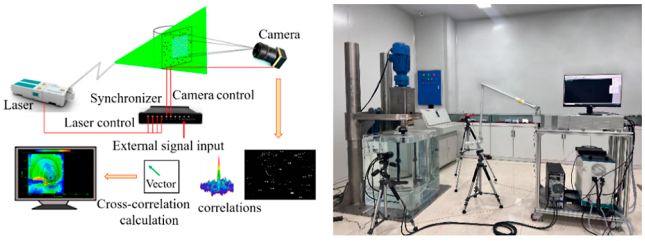

(a) PIV test principle (b) PIV Experimental Apparatus

Figure 2. PIV test system.

constant measurement phase, an electromagnetic phase locking device is used, and the blade angular position, light source, and image acquisition are synchronized. In the solid−liquid two-phase flow field of the PIV experiment, with the corresponding filters, liquid flow can be tested when the light source is a laser, and particle flow can be tested when the light source is an LED. The tracer particles in this experiment are fluorescent particles, and the solid particles are hollow glass beads. The liquid is pure water (distilled water). The parameters of the liquid and solid particles are shown in Table 1.

A standard elliptical-bottomed mixing tank made of transparent Plexiglas with dimensions schematically shown in Supporting Information Figure S1 was used for the study.

https://doi.org/10.1021/acsomega.3c05762
ACS Omega 2023, 8, 47635−47645

Table 1. Physical Properties Parameters

parameter	symbol	value
liquid density	ρ_L	1000 kg/m^3
hydrodynamic viscosity	μ	0.001 Pa·s
solid particles density (glass beads)	ρ_S	1430 kg/m^3
solid particles diameter	d_S	0.15 mm
solid volume fraction	φ_S	5.6%
tracer particle volume fraction	φ_T	1%

Table 2 shows the dimensions of the tank. The mixing tank is placed inside a square water box container to minimize the optical refractive index effect on its cylindrical surface.

Table 2. Structural Parameters of the Mixing Tank and Impeller

parameter	symbol	value
tank diameter	T	500 mm
liquid height	H	1.6 T
baffle width	W_b	0.08 T
baffle height	h	1.35 T
impeller diameter	D	0.5 T
off-bottom clearance	C	0.35 T
impeller spacing	S	0.65 T

2.2. Computational Simulation Methodology.

2.2.1. Mathematical Model. In this study, the Eulerian–Eulerian multiphase flow model is used to simulate the flow of two phases, each of which is considered a mutually coherent continuum, in order to solve the Reynolds-averaged continuity equation and the momentum conservation equation for each phase. The controlling equations for phase q (liquid phase q = l, solid phase q = s) are as shown below:[25]

Continuity equation

$$\frac{\partial}{\partial t}(\alpha_q\rho_q)+\nabla\cdot(\alpha_q\rho_q u_q)=0 \tag{1}$$

where α_q is the volume fraction of the q-phase, u_q is the velocity of the q-phase, and ρ is the density of the q-phase.

Liquid phase momentum conservation equation

$$\frac{\partial}{\partial t}(\alpha_l\rho_l u_l)+\nabla\cdot(\alpha_l\rho_l u_l u_l) = -\alpha_l\nabla p_l+\nabla\cdot\bar{\bar{\tau}}_l - K(u_l-u_s)+\alpha_l\rho_l g \tag{2}$$

where p_1 is the thermal motion pressure, g is the gravitational acceleration, $\bar{\bar{\tau}}$ is the viscous stress tensor of the liquid phase, and K is the interphase momentum transfer coefficient.

Solid phase momentum conservation equation

$$\frac{\partial}{\partial t}(\alpha_s\rho_s u_s)+\nabla\cdot(\alpha_s\rho_s u_s u_s) = -\alpha_s\nabla p - \nabla p_s+\nabla\cdot\bar{\bar{\tau}}_s - K(u_l-u_s)+\alpha_s\rho_s g \tag{3}$$

where $\bar{\bar{\tau}}_s$ is the viscous stress tensor of the solid phase and p_s is the solid phase pressure.

$\bar{\bar{\tau}}_s$ is related to the solid phase dynamic viscosity μ_s, the solid phase pressure p_s, and the shear viscosity λ_s, for which the particle kinetic theory is used to calculate:

The pressure of the solid phase is

$$p_s = \alpha_s\rho_s\theta_s+2\rho_s(1+e_{ss})\alpha_s^2 g_{0,ss}\theta_s \tag{4}$$

where e_{ss} is the inelastic collision recovery coefficient of particles, θ_s is the temperature of particles, $g_{0,ss}$ is the radial distribution function of particles, and is calculated by the following equation

$$g_{0,ss} = \left[1-\left(\frac{\alpha_s}{\alpha_{s,max}}\right)^{1/3}\right]^{-1} \tag{5}$$

The solid phase shear viscosity is

$$\lambda_s = \frac{4}{5}\alpha_s^2\rho_s d_s g_{0,ss}(1+e_{ss})\sqrt{\frac{\theta_s}{\pi}} + \frac{10\rho_s d_s\sqrt{\pi\theta_s}}{96\alpha_s(1+e_{ss})g_{0,ss}}\left[1+\frac{4}{5}g_{0,ss}\alpha_s(1+e_{ss})\right]^2 \tag{6}$$

The solid phase kinetic viscosity is

$$\mu_s = \frac{4}{5}\alpha_s^2\rho_s d_s g_{0,ss}(1+e_{ss})\sqrt{\frac{\theta_s}{\pi}} \tag{7}$$

In this study, a k-ε mixed turbulence model is used to calculate the turbulent kinetic energy and dissipation rate of the liquid phase, assuming that both phases have the same k and ε. The k and ε equations describing the model are as follows

$$\frac{\partial}{\partial t}(\rho_m k)+\nabla\cdot(\rho_m u_m k) = \nabla\cdot\left(\mu_m+\frac{\mu_{t,m}}{\sigma_k}\nabla k + G_{k,m}+G_{b,m}-\rho_m\varepsilon\right) \tag{8}$$

$$\frac{\partial}{\partial t}(\rho_m \varepsilon)+\nabla\cdot(\rho_m u_m \varepsilon) = \nabla\cdot\left(\frac{\mu_{t,m}}{\sigma_\varepsilon}\nabla\varepsilon\right)+\frac{\varepsilon}{k}(C_{1\varepsilon}G_{k,m}-C_{2\varepsilon}\rho_m\varepsilon) \tag{9}$$

where ρ_m is the mixture density, μ_m is the molecular viscosity, and u_m is the velocity.

While neglecting the effects of virtual mass force, lift force, and mass transfer, the study primarily focuses on the significant impact of drag force on simulation results.[26] The momentum exchange coefficients are calculated using the Huilin-Gidaspow model.

Resistance is a key factor affecting the behavior of solid-phase and liquid-phase flow in a stirred tank.[19] The Gidaspow model, which combines the Wen-Yu model for a low solid-phase charging rate and the Ergun model for a high solid-phase charging rate, has been widely used in the simulation of gas–solid two-phase flow.[26] Huilin et al.[27] further improved the Gidaspow model by using the smoothing function and obtained the Huilin-Gidaspow model with better continuity in the transition from low to high solid volume fraction, which was used to calculate the interfacial momentum transfer coefficient

$$\bar{K} = (1-\psi)K_E+\psi K_{WY} \tag{10}$$

where ψ is the smoothing function with the following expression

$$\psi=\frac{\arctan[150\times 1.75(0.2-\alpha_s)]}{\pi}+0.5 \tag{11}$$

https://doi.org/10.1021/acsomega.3c05762
ACS Omega 2023, 8, 47635−47645

$$K_E = 150\frac{(1-\alpha_l)^2\mu_l}{(\alpha_l d_s)^2} + 1.75\frac{\rho_l(1-\alpha_l)|u_l - u_s|}{\alpha_l d_s}\alpha_l \le 0.8 \quad (12)$$

$$K_{WY} = \frac{3}{4}C_D\frac{\rho_l(1-\alpha_l)|u_l - u_s|}{d_s}\alpha_l^{-2.65}\alpha_l > 0.8 \quad (13)$$

$$C_D = \frac{24}{\alpha_l Re_s}[1 + 0.15(\alpha_l Re_s)^{0.687}] \quad (14)$$

$$Re_s = \frac{\rho_l d_s|u_s - u_l|}{\mu_l} \quad (15)$$

where ψ is the smoothing function, $\overline{K}$ is the fluid-solid exchange coefficient, Re_s is the relative Reynolds number, and C_D is the drag function.

2.2.2. Computational Grids and Numerical Details. The mesh delineation should consider the geometric model, computational capability, and computational time. The accuracy of numerical simulation results is greatly influenced by mesh quality, with particular significance in the case of a rotating impeller within the mixing tank. Proper modeling and mesh delineation of the impeller influence zone, as well as the remaining impeller region, can significantly affect the computational outcomes. The simulation in this study uses the multiple frames of reference method to emulate the strong rotational, pulsating, and nonlinear nature of the impeller zone; therefore, the computational region needs to be divided after the geometric model is built. The overall mesh of the mixing tank is shown in Figure 3a.

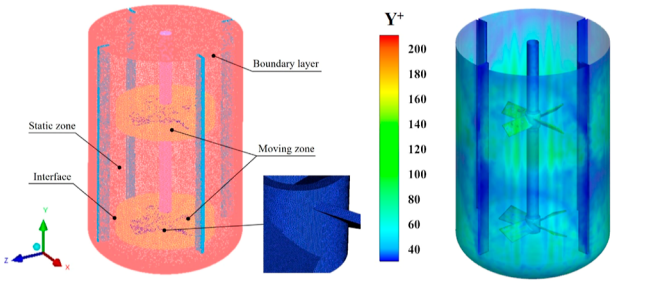

(a) In-tank watershed gird (b) Distribution of wall Y^+ values

Figure 3. Mixing tank meshing.

In the prediction of wall turbulence, the near-wall grid resolution can be evaluated by Y^+, which is usually defined as follows

$$Y^+ = \frac{u_\tau x}{\nu} \quad (16)$$

where u_τ is the shear velocity of the liquid near the wall, x is the distance from the wall, and ν is the kinematic viscosity. The region where $Y^+ < 5$ is called the viscous sublayer with a nonlinear form of velocity, and the region where $Y^+ > 60$ is the fully developed turbulent flow, also called the logarithmic law region, with a basically linear trend of velocity and distance, and the region in between is called the transition sublayer. The calculations in this paper ensure that the Y^+ value of the wall meets $30 < Y^+ < 300$, which satisfies the requirements of the standard wall function. The Y^+ value of the wall surface is shown in Figure 3b.

The correct setting of initial and boundary conditions is crucial to ensure the accuracy of numerical simulation results. The simulated liquid and solid phases are water and solid glass beads, respectively, and the physical parameters are shown in Table 1. In the initial state, solid particles are deposited at the bottom of the mixing tank while the liquid remains stationary. The near-wall surface is represented by the standard wall function; the stirring shaft and impeller are set as the moving wall, while the rest of the geometric walls are supposed to have no-slip boundary conditions, and the top is set as a symmetric boundary condition to simulate the effect of a free liquid surface. A time step of 0.001 s is used, and for the simulation, 100 revolutions are sufficient to reach the steady-state condition.[28]

The two-phase control equations are solved in a double-precision solver using the commercial CFD software FLUENT. The Eulerian model is used to study the solid−liquid two-phase flow, and the solution method is the pressure-based transient implicit approach. The diffusion and convection terms are discretized in the central difference format and the second-order upwind scheme, respectively. Due to the large computational effort, a high-performance computing cluster is used for the calculations. Utilizing the Sunway TaihuLight supercomputing cluster, it achieves a peak computational performance of over 100 PFLOPS and can concurrently handle up to 24 computational tasks.[19]

2.3. Geometric Data Modeling Methodology. As a key component affecting the flow characteristics in the tank, the structural characteristics of the stirrer greatly affect the mixing performance of the two-phase media. As the dual-impeller stirred tank studied in this paper, the impeller geometry size, impeller spacing, and off-bottom spacing all affect the particle suspension effect, and usually, the impeller spacing and off-bottom spacing are difficult to adjust due to the shaft hole and motor settings.

Therefore, this paper adopts the following method to describe the lower and upper impeller geometry dimensions. As shown in Figure 4 is the blade geometry size schematic B_u is the upper impeller width, B_{lo} is the lower impeller outer edge width, B_{li} is the lower impeller inner edge width, θ_u is the upper impeller bevel angle, θ_{lo} is the lower impeller outer edge bevel angle, θ_{li} is the lower impeller inner edge bevel angle, δ_u is the upper impeller thickness, δ_{lo} is the lower impeller outer edge thickness, and δ_{li} is the lower impeller inner edge thickness. To

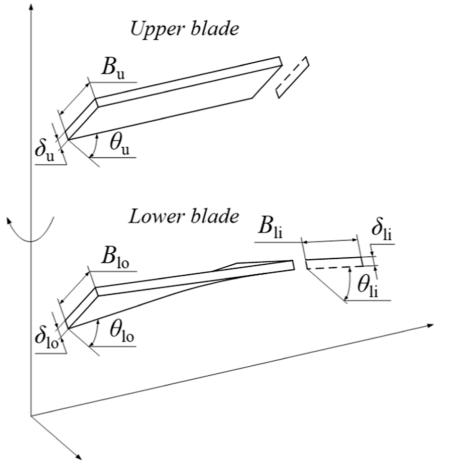

Figure 4. Geometric parameters of the upper and lower impellers.

https://doi.org/10.1021/acsomega.3c05762
ACS Omega 2023, 8, 47635−47645

reduce the calculation time, the control variables are in a certain range. According to the prototype geometry and engineering experience, the variation range of parameters is set, B_u = 30−50 mm, B_{lo} = 55−75 mm, B_{li} = 35−55 mm, θ_u = 40−50°, θ_{lo} = 15−35°, θ_{li} = 35−55°, δ_u = 3−6 mm, δ_{lo} = 2−5 mm, δ_{li} = 3−6 mm.

2.4. Global Sensitivity Analysis and Optimization Methodology. In the study of solid−liquid two-phase mixing systems, Zwietering[29] proposed the criterion of complete suspension, i.e., no particles are retained at the bottom of the tank for more than one second. This theory is widely used and developed, but in the numerical simulation and experimental study of this research, this feature is difficult to observe and quantitatively characterize, which is not suitable for the multiobjective optimization study of this paper.

In the upper part of the stirred tank, there is a clear layered interface between the transparent liquid and suspended solids, and the height of this interface is defined as the cloud height. Kraume[30] indicated that the cloud height reaches 90% of the liquid height when it reaches a fully suspended state. Therefore, the cloud height can be used as an important parameter to evaluate the mixing degree, which is defined in this paper as the maximum axial height of the mean solid.

The above impeller geometry parameters were used as input variables, and cloud height and shaft power were used as output values. We trained the RBF models using the results of sensitivity analysis obtained through the Sobol method. These models are fine-tuned and optimized using the Genetic Algorithm (GA). The models accurately reflect the variation relationship between the geometric parameters and target parameters. The above work is mainly done in MATLAB, as detailed below:

The DOE sampling was performed by the optimal Latin hypercube design method in this paper. The approximation model was established by combining the sample data of 55 sets of variables and the corresponding responses obtained from numerical simulation calculations. The first 50 groups of them were taken as the sample matrix data, and the last five groups were taken as the test data.

RBF models typically utilize training data to determine the values of the center points c and weights w in order to fit the relationship between input features and output, as expressed in the following equation.

$$f(x)=\Sigma\varphi(||x - c||)\times w \tag{17}$$

We use a global sensitivity analysis (GSA) method based on Sobol's approach, which reflects the influence of uncertainties on the output over the entire variation space.[31] Sobol's method is a variance-based global sensitivity calculation approach that decomposes the system output variance into the sum of the variances determined by each input variable. The overall variance D_0 of Sobol's method is the ensemble of the contributions of the individual non-normalized variance components D_a.

$$D_0 = \int_\Omega f(x)^2 \mathrm{d}F(x) - f_a^2 \tag{18}$$

During the simulation process, the fundamental equation for calculating the power of the rotating machinery is based on vorticity. The equation for calculating the power of the rotating machinery can be expressed as follows. Where $\mathbf{v}$ is the fluid velocity vector, $\mathbf{r}$ is the position vector, and $\mathbf{V}$ stands for vorticity.

$$P = \iiint (\rho\cdot\mathbf{v}\cdot\mathbf{r}\times\mathbf{V})\cdot\mathrm{d}V \tag{19}$$

The cloud height is obtained through postprocessing based on the average solid-phase concentration. Calculating the average concentration typically involves the mass conservation equation and integral operations. The equation for calculating the average concentration can be expressed as follows. Where V is the calculated region's volume and $C(\mathbf{r})$ is associated with the concentration field function related to position vectors.

$$C_{av} = \frac{1}{V}\int_V C(\mathbf{r})\mathrm{d}V \tag{20}$$

The approximate functions obtained by RBF were analyzed for sensitivity using the Sobol method, and the global sensitivity parameters of various influence factors were solved. The global sensitivity reflects not only the degree of effect of an individual influencing factor on the stirring cloud height and shaft power but also the interaction effect with other influence factors.

Sensitivity analysis serves as an initial step in optimization, while optimization based on sensitivity analysis represents a subsequent stage. The primary objective of the initial optimization is sensitivity analysis, which aims to narrow the relevant geometric parameter values and ranges affecting the optimal design. Subsequently, the second optimization phase further refines the structure based on sensitivity analysis outcomes. Sensitivity analysis not only identifies crucial parameters impacting target performance but also streamlines computations and the overall project complexity.

In the initial optimization, all nine parameters are considered as design variables, with cloud height H_c and shaft power P as optimization objectives as described by eq 21. Subsequently, in the postsensitivity analysis optimization, the four variables with the most significant impact on cloud height and shaft power are chosen as design variables, with cloud height and shaft power remaining as optimization targets, defined by eq 22.

$$\begin{cases} \max(H_c(B_u, B_{lo}, B_{li}, \theta_u, \theta_{lo}, \theta_{li}, \delta_u, \delta_{lo}, \delta_{li})) \\ \min(P(B_u, B_{lo}, B_{li}, \theta_u, \theta_{lo}, \theta_{li}, \delta_u, \delta_{lo}, \delta_{li})) \\ 30 \le B_u \le 50;\ 55 \le B_{lo} \le 75;\ 35 \le B_{li} \le 55 \\ 40 \le \theta_u \le 50;\ 15 \le \theta_{lo} \le 35;\ 35 \le \theta_{li} \le 55 \\ 3 \le \delta_u \le 6;\ 2 \le \delta_{lo} \le 5;\ 3 \le \delta_{li} \le 6 \end{cases} \tag{21}$$

$$\begin{cases} \max(H_c(B_{lo}, \theta_{lo}, \theta_{li}, \delta_{lo})) \\ \min(P(B_{lo}, \theta_{lo}, \theta_{li}, \delta_{lo})) \\ 65 \le B_{lo} \le 75;\ 15 \le \theta_{lo} \le 25 \\ 45 \le \theta_{li} \le 55;\ 2 \le \delta_{lo} \le 3.5 \end{cases} \tag{22}$$

Using NSGA-II (Nondominated Sorting Genetic Algorithm-II) to solve the sensitivity analysis-based RBF model, we ultimately achieve the desired optimization results. GAs are optimization techniques based on principles inspired by biological evolution. Within the optimization process, information accumulates naturally in the search space, resulting in the emergence of the most favorable solutions. NSGA-II, an improvement over the original NSGA, introduces two pivotal concepts: fast nondominant sorting and crowding sorting. Fast nondominant sorting efficiently generates sets of nondominant solutions, also referred to as Pareto optimal solutions, in each

https://doi.org/10.1021/acsomega.3c05762
ACS Omega 2023, 8, 47635−47645

generation.[32] Due to the relatively small parameter group size involved in this design, a crossover rate of 0.8 and a mutation rate of 0.01 were selected. This choice aims to maintain diversity within the population while avoiding premature convergence.

3. RESULTS AND DISCUSSION

3.1. Model Validation and Prototype Impeller Analysis. In this study, PIV experiments were used to verify the accuracy of the numerical model. At higher impeller speeds, the transparency of the system is severely affected (a large number of air bubbles at high rotational speeds), which largely affects the employment of optical experimental methods such as PIV. Therefore, the impeller speed was set to 120 rpm, and PIV experiments and CFD numerical simulations were performed under uniform conditions. The simulation and experimental conditions were kept the same in this study.

Figure 5 shows a comparison of the liquid phase flow fields from the PIV experiments and CFD simulations, both

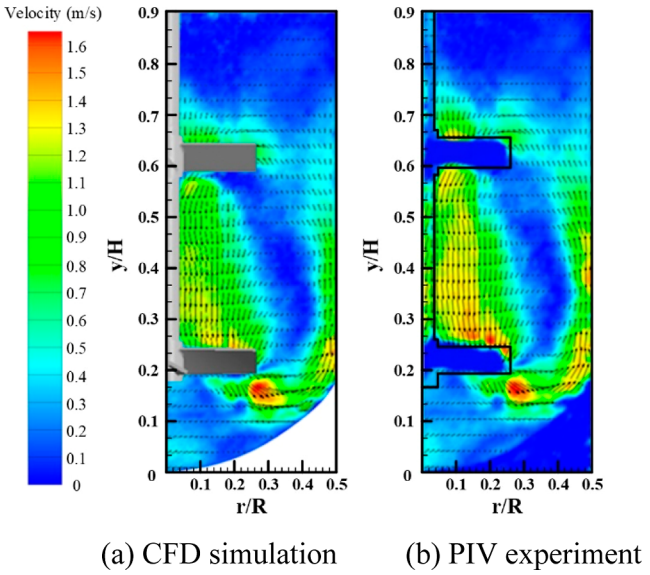

Figure 5. Average flow field of liquid phase.

predicting the presence of a circulation loop in the tank. The lower impeller produces mainly bottom-up axial circulation near the wall surface, while the upper impeller enhances mainly top-down axial circulation near the shaft end. The impeller rotation generates high-speed jets with a high flow velocity in the impeller region and low velocity in the upper and bottom of the mixing tank. The numerical simulation results are consistent with the PIV experimental results, which prove that the numerical model is reliable. The average flow field of the liquid phase.

In order to verify the grid independence, the simulation results for different numbers of grids were compared with the test data of PIV. Figure 6 displays the axial distribution of the liquid phase velocity for three different grid quantities (900k, 1500k, and 2000k), with the axial plane located at y = 0.2H. From the figure, it can be found that the results of different grid numbers have the same trend, but the CFD results of 900k grids have a large deviation from the PIV experimental data. To obtain accurate results, further refinement of the grids is needed. The velocities obtained from numerical simulations with 1,500,000 grids and 2,000,000 grids are similar to the

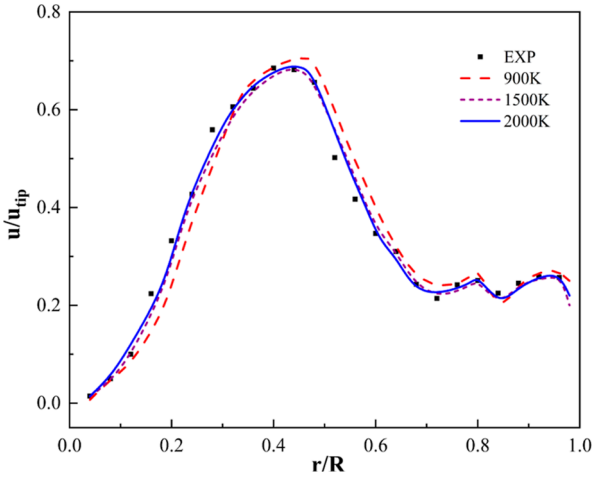

Figure 6. Comparison of average fluid flow velocity with experimental values for different grid numbers at y = 0.2H.

experimental results, and the relative errors are less than 5%. It shows that the numerical emulation can reasonably forecast the complex flow in the mixing tank. Therefore, 1,500,000 grids are used in all subsequent simulations to accomplish a tradeoff between computational cost and simulation accuracy.

For the solid−liquid dual-impeller stirred tank, its internal flow field characteristics are complex, with vortex system structure, circulating flow structure, two-phase mixing structure, etc., which exhibit strong three-dimensional non-constant characteristics.

The quantitative analysis of the solid volume fraction is essential to study the mixing performance. Figure 7 shows the

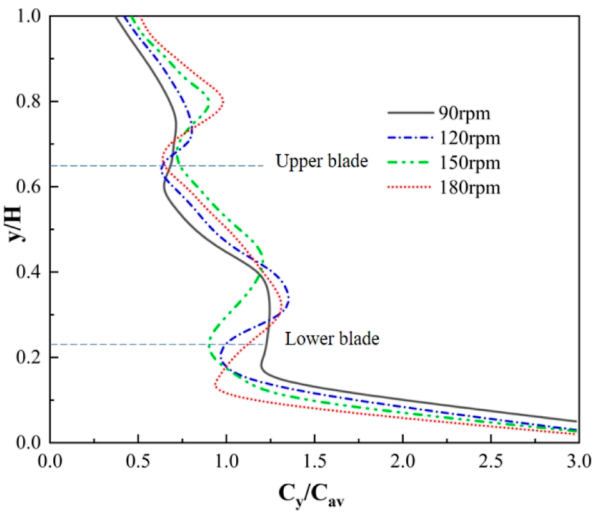

Figure 7. Local axial solids concentration distribution at different stirring speeds at r = 0.2R.

axial solid phase volume fraction distribution at different impeller speeds for the prototype impeller. The y-axis is normalized with reference to the center height. The average solid phase concentration of Cav is 5.6%. As shown in the figure, particles accumulate at the bottom of the mixing tank, well above the average, while the top is clear with fewer particles and below the average. Due to the axial circulation effect of the double impeller, there is a discrepancy in the flow field near the impeller. The particle content above the impeller

https://doi.org/10.1021/acsomega.3c05762
ACS Omega 2023, 8, 47635−47645

is slightly higher than that below the impeller. As the stirring speed increases, the suspension of particles in the tank becomes significantly better.

3.2. Optimized Impeller Design and Experimental Validation. Calculations indicate that the optimized geometric parameters for the relevant section are shown in Supporting Information Table D1. A comparison of the numerical simulation and surrogate model prediction results is presented in Supporting Information Table D2. In Table D2, H_{c1} and P_1 represent the numerical simulation results, while H_{c2} and P_2 represent the surrogate model prediction results. The calculated MAE value for cloud height is 4.18 with an R^2 value of 0.97, and for power, the MAE value is 2.57 with an R^2 value of 0.98. These results indicate that the model's predicted data closely aligns with the simulation data, demonstrating relative accuracy in the model's predictions.

Figure 8 shows the results of the GSA. The GSA shows that among the nine input variables, the lower impeller outer edge

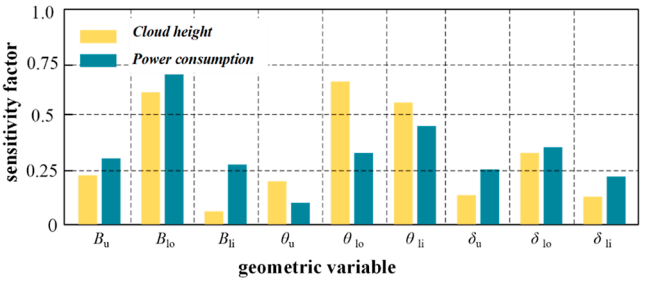

Figure 8. Impact factors of the different variables.

width B_{lo}, the lower impeller outer edge bevel angle θ_{lo}, the lower impeller inner edge bevel angle θ_{li}, and the lower impeller outer edge thickness δ_{lo}, which are the four variables that have a greater degree of influence on the cloud height and power consumption. Therefore, based on the first optimal results, the sampling interval is narrowed, and the second sampling is performed and optimized while keeping the parameters of upper impeller width B_u, lower impeller inner edge width B_{li}, upper impeller bevel angle θ_u, upper impeller thickness δ_u, and lower impeller inner edge thickness δ_{li} unchanged.

The built RBF model is solved using NSGA-II to obtain the normalized Pareto solution set, as shown in Figure 9. The power consumption is normalized by the maximum power of the motor (P_{max} = 2000 W). The cloud height is normalized by the maximum height of the liquid level, and the vertical coordinate in the graph is the reciprocal of the cloud height to clearly show the relationship between the power consumption and cloud height variation.

In this article, cloud height and power are considered equally important, and the red dot in the figure is marked as the optimal solution selected in this paper.

Studying the characteristics of the impeller wake vortex is essential to optimize the performance of the mixing tank. As shown in Figure 10, a trailing vortex was generated at the tip of each blade before and after optimization. During the suspension of solid phase particles, most of the blade energy is expended in the wake vortex, and very little can be transferred to the far end of the flow field.[33] As shown in Figure 12, the large size and narrow shape of the wake vortex near the original impeller are not conducive to energy transfer. However, the optimized impeller can observably influence the

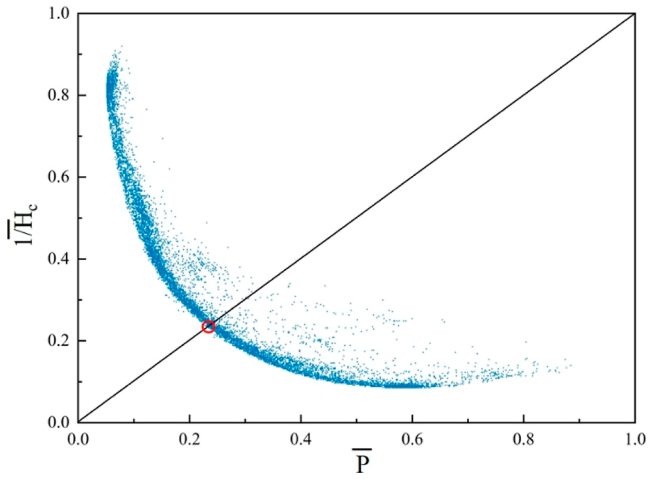

Figure 9. Normalized Pareto solution set.

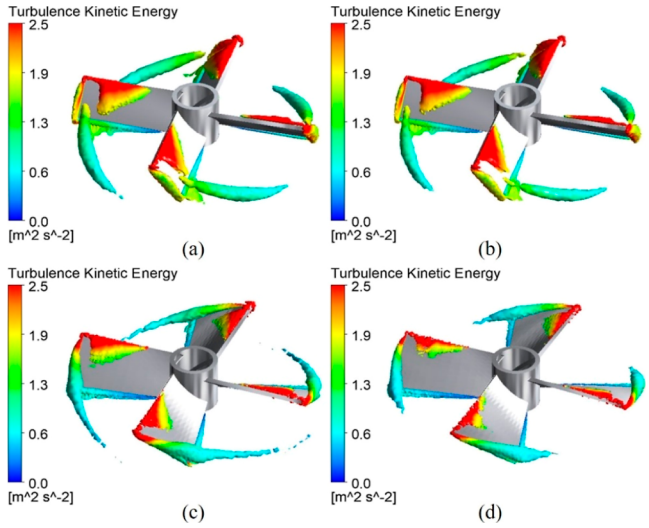

Figure 10. Numerical simulation results of blade tail vortex dissipation structure: (a) original upper impeller, (b) optimized upper impeller, (c) original lower impeller, and (d) optimized lower impeller.

wake vortex structure. The large size of the wake vortices at the tail of the original blades is displaced by the smaller wake vortices of the new impeller. Moreover, the relatively low pressure at the focus of these swirls provides an additional driving force to the impeller, which reduces the energy consumption to some extent. As shown in Table 3, keeping other parameters unchanged under the design conditions and changing only the fluid viscosity, it is found that the optimized impeller has lower power consumption compared with the original impeller under different viscosities.

Turbulence parameters play an important role in improving the quality of solid−liquid suspension and reducing the mixing time. Turbulent kinetic energy is a measure of the flow field fluctuation, which is the sum of the root-mean-square of the velocity fluctuation and reflects the mixing performance of the impeller.[34] The time-averaged distributions of turbulent kinetic energy and turbulent kinetic energy dissipation rate before and after optimization are given in Figure 11, and their values are normalized from the blade tip velocity u_{tip}.

Generally, the turbulent and turbulent energy dissipation rates are larger near the impeller tip and lower away from the

https://doi.org/10.1021/acsomega.3c05762
ACS Omega 2023, 8, 47635−47645

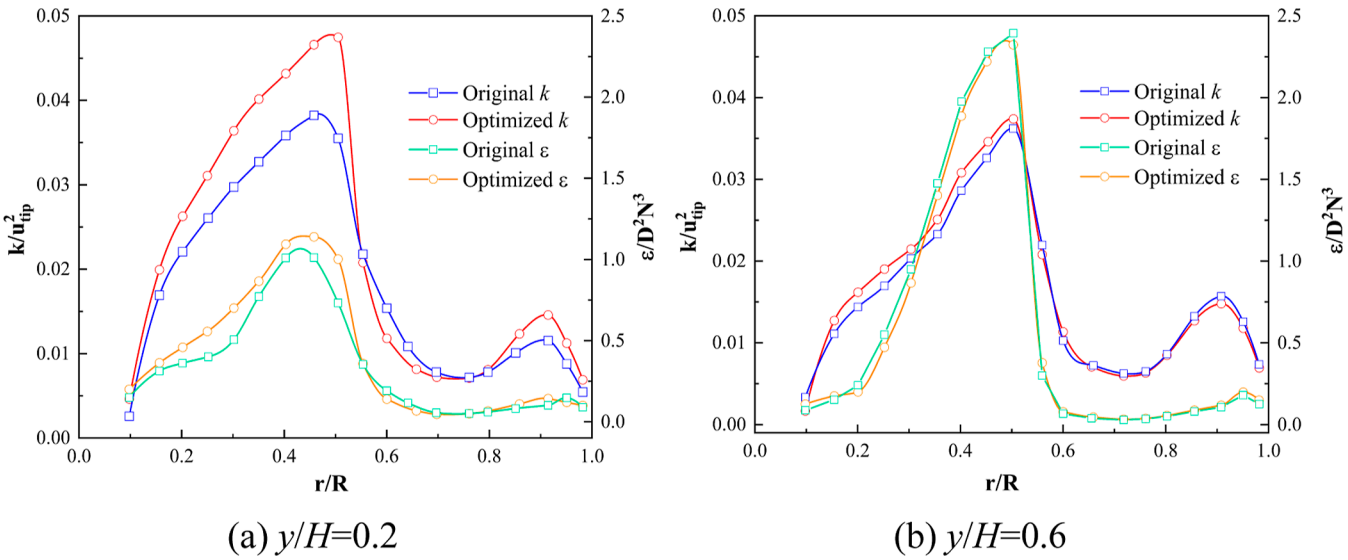

Figure 11. Turbulent kinetic energy and turbulent energy dissipation rate distribution.

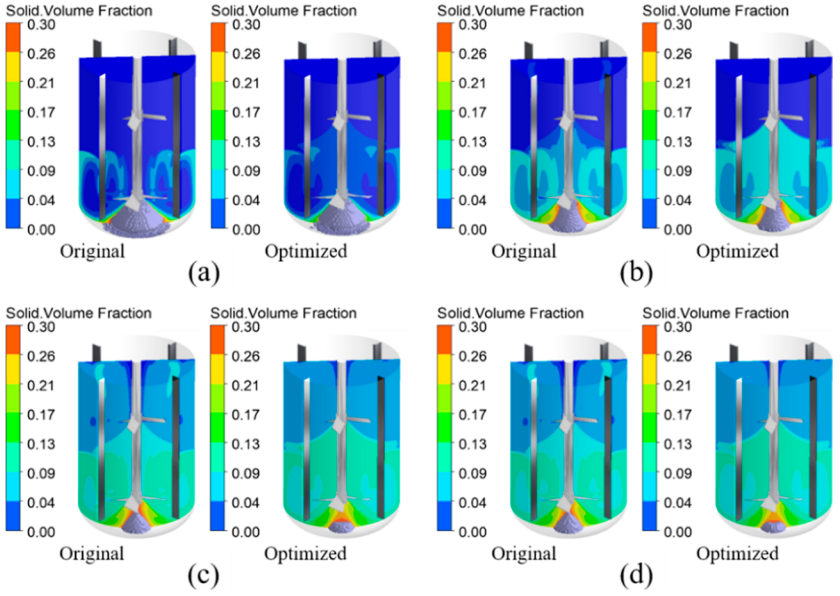

Figure 12. Particle deposition distribution: (a) $t = T_0$, (b) $t = 2T_0$, (c) $t = 3T_0$, and (d) $t = 4T_0$.

Table 3. Dual-Impeller Power Consumption for Different Fluid Viscosity Conditions

viscosity (Pa·s)	0.001	0.005	0.01	0.03
original P (W)	573.0	742.3	939.6	1307.4
optimized P (W)	483.6	638.1	815.5	1176.9

rotating region. The optimized impeller increased the turbulent kinetic energy to some extent, while the turbulent dissipation rate did not change much. The higher the turbulent kinetic energy, the more intense the motion of the fluid and particles. The turbulent dissipation rate is approximately constant, and the energy loss is low. Increasing the turbulent energy can improve the macroscopic mixing of the liquid phase, thus improving the suspension of the solid phase. This is due to the change in the degree of curvature of the lower impeller and the thickness of the tip of the blade after optimization, which significantly enhances the discharge capacity of the blade and leads to an increase in vortex diffusion and turbulence intensity.

When the solid-phase mass fraction within a region reaches the critical density, particles in that area are considered to have sedimented. Figure 12 shows the distribution of particle deposition in the mixing tank at different moments before and after the optimization, T_0 is a mixing cycle corresponding to the actual calculation time of 10 s, and the mixing cycle is controlled to be consistent in order to compare the mixing effect. It can be found that the deposition region of the particles is mainly located below the impeller. This result shows that the optimized impeller creates a stronger circulating flow field in the blade region, takes less time to reach a fully suspended state, and deposits fewer particles at the bottom of the tank.

It can also be seen from Supporting Information Figure S2 that the solid-phase concentration curves inside the stirred tank were smoother after optimization, and the solid-phase concentration gradients were all reduced to different degrees.

https://doi.org/10.1021/acsomega.3c05762
ACS Omega 2023, 8, 47635−47645

This indicates that the solid-phase uniformity in the optimized stirred tank has been improved, with the most obvious improvement in solid−liquid mixing uniformity at r = 0.1−0.5R. This is due to the more reasonable design of the optimized impeller geometry, which can give full play to the advantages of the double impeller mixing tank. The geometry strengthens the fluid transfer, destroys the symmetric structure of the flow field, and enhances the fluid transfer effect between the blades, all of which help to improve the mixing performance of the system.[35]

Figure 13 shows the mean particle concentration iso-surfaces and their projections before and after optimization, with the

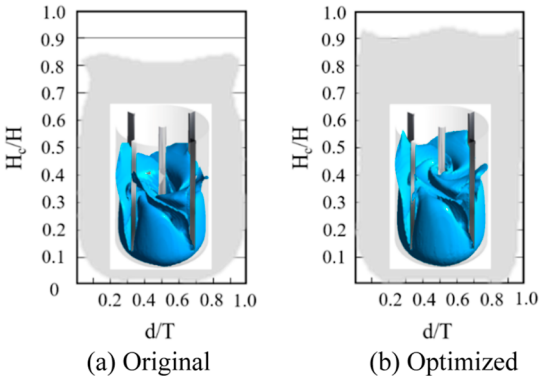

Figure 13. Iso-surfaces of mean particle concentration and their projections.

height of the projected maximum and for the cloud height. It is evident from the figure that after optimization, the cloud height has increased compared to the preoptimization state, indicating a greater suspension of particles at higher positions. The cloud height in the full vessel after optimization has reached more than 90% of the liquid height, which has reached the full suspension according to the criteria of Kraume.[30]

The impeller parameters of the optimal solution can be obtained by consulting Supporting Information Table D3. At the design operating point, the optimization results in an 8.7% increase in cloud height and a 15.6% decrease in power compared to the prototype stirred tank. The 3D-printed model of the impeller is shown in Figure 14. The upper impeller exhibits no significant changes compared with the prototype, representing minor geometric optimizations. In contrast, the lower impeller undergoes substantial modifications, constituting major geometric optimizations.

PIV experiments were performed using the optimized impeller. Figure 15 shows the volume fraction distribution of particles in the stirred tank before and after the optimization. It is not difficult to see that the degree of particle accumulation at the bottom of the optimized stirred tank is significantly reduced (the particles used in the PIV experiment are spherical glass beads, so the accumulation form is not conical accumulation but spread-out accumulation), and the upper clear liquid area is significantly reduced. Therefore, the two-phase mixing effect in the optimized mixing tank is significantly better than the prototype, and the optimized results are reliable.

4. CONCLUSIONS

In this study, the multiobjective optimal design of a solid−liquid dual-impeller mixing tank was carried out based on the

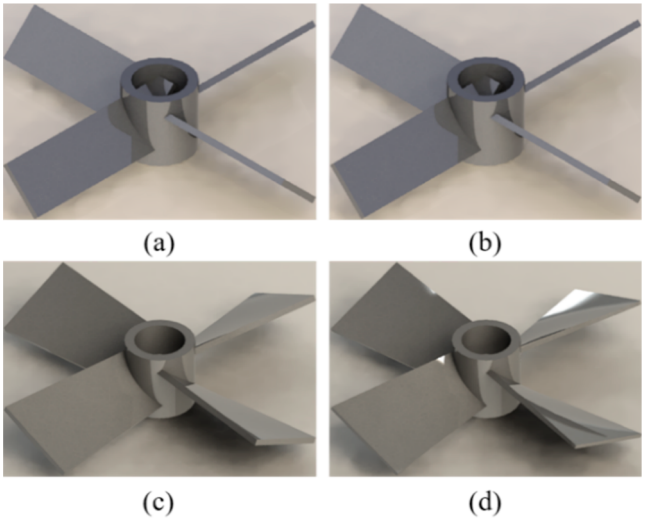

Figure 14. 3D-printed model of impeller before and after optimization: (a) original upper impeller, (b) optimized upper impeller, (c) original lower impeller, and (d) optimized lower impeller.

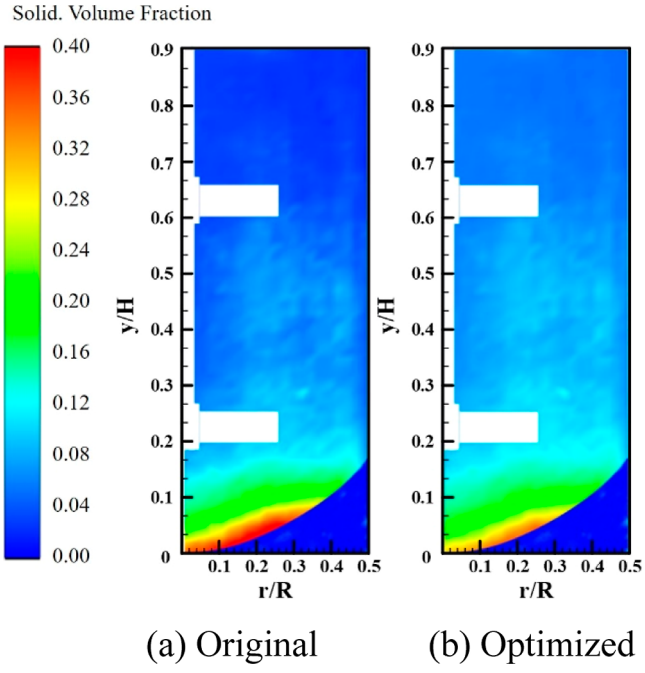

Figure 15. Volume fraction of solid particles measured by the PIV experiment.

RBF approximation model and Sobol's sensitivity method, and the feasibility and effectiveness were verified by numerical simulation and a PIV experimental study. The main conclusions are as follows:

The accurate numerical simulation and experimental analysis of the stirred tank revealed that the optimized stirred tank's solid−liquid mixing performance and particle suspension performance were significantly improved, while the power consumption was reduced. The final optimized result of the studied dual-impeller stirred tank under the design working conditions increased the cloud height by 8.7% and reduced the power consumption by 15.6% relative to the prototype.

The parametric method is applied to the optimal design of the dual-impeller mixing tank, and the influence weights of

https://doi.org/10.1021/acsomega.3c05762
ACS Omega 2023, 8, 47635−47645

each influencing factor on the cloud height and power consumption are determined by Sobol's method. Based on the GSA, four variables with greater influence factors on the cloud height and power consumption of the solid−liquid stirred tank were identified for the postsensitivity analysis optimization. The coupling relationship between parameters and response is clarified under the premise of more design variables, and a new idea is provided to optimize the design of solid−liquid dual-impeller stirred tanks and other stirred tanks. The optimization process is logical and reasonable and has engineering application value, which can be extended to the optimal design of similar fluid machinery.

■ ASSOCIATED CONTENT

Supporting Information

The Supporting Information is available free of charge at https://pubs.acs.org/doi/10.1021/acsomega.3c05762.

> Dual-impeller mixing tank dimensions, axial distribution of solid-phase concentrations at different radial positions (r = 0.1 ∼ 0.9R), dual-impeller blade geometry parameters summary table, numerical simulation results and proxy model predictions for cloud height and power, and design variables and objective function values before and after optimization (PDF)

■ AUTHOR INFORMATION

Corresponding Author

Shuiqing Zhou − *College of Mechanical Engineering, Zhejiang University of Technology, Hangzhou 310023, China; Institute of Innovation Research of Shengzhou, Zhejiang University of Technology, Shengzhou 312400, China*; Email: zsqwh986@zjut.edu.cn

Authors

Ding Xia − *College of Mechanical Engineering, Zhejiang University of Technology, Hangzhou 310023, China; Institute of Innovation Research of Shengzhou, Zhejiang University of Technology, Shengzhou 312400, China*; orcid.org/0009-0003-1158-9172

Zijian Mao − *College of Mechanical Engineering, Zhejiang University of Technology, Hangzhou 310023, China; Institute of Innovation Research of Shengzhou, Zhejiang University of Technology, Shengzhou 312400, China*

Xing He − *College of Law, Zhejiang University of Technology, Hangzhou 310023, China*

Yixi Wang − *College of Mechanical Engineering, Zhejiang University of Technology, Hangzhou 310023, China; Institute of Innovation Research of Shengzhou, Zhejiang University of Technology, Shengzhou 312400, China*

Complete contact information is available at: https://pubs.acs.org/10.1021/acsomega.3c05762

Author Contributions

The manuscript was written with the contributions of all authors. All authors have given their approval to the final version of the manuscript. Ding Xia: Conceptualization, Writing—Original draft preparation; Zijian Mao: Data curation, Methodology; Shuiqing Zhou: Visualization, Investigation, Experimental test; Xing He: Software, Writing—review and editing; Yixi Wang: project administration.

Funding

This research was funded by the National Natural Science Foundation of China, grant number 51706203, and the Natural Science Foundation of Zhejiang Province, grant number LY20E090004.

Notes

The authors declare no competing financial interest.

■ ACKNOWLEDGMENTS

This research was supported by the National Natural Science Foundation of China (grant no. 51706203) and the Natural Science Foundation of Zhejiang Province, exploration project (Y, LY20E090004). Thanks to ZJUT for providing computing resources and technical support. The authors also appreciate all other scholars for their advice and assistance in improving this article.

■ NOMENCLATURE

B_{li}	lower impeller inner edge width, mm
B_{lo}	lower impeller outer edge width, mm
B_u	upper impeller width, mm
C	off-bottom clearance, mm
C_{av}	average solid phase concentration
C_D	drag function
C_y	axial solid phase concentration
D	impeller diameter, mm
D_0	overall variance of Sobol's method
D_a	individual non-normalized variance component
d_s	solid particles diameter, mm
e_{ss}	particles inelastic collision recovery coefficient
g_{0ss}	particles radial distribution function
g	gravitational acceleration, m/s^2
H	liquid height, mm
H_c	cloud height, mm
h	baffle height, mm
k	turbulent energy, m^2/s^2
K	interphase momentum transfer coefficient
p	phase pressure, Pa
S	blade spacing, mm
T	tank diameter, mm
T_0	mixing time
Re_s	relative Reynolds number
u_{tip}	velocity of blade tip, m/s
W_b	baffle width, mm

■ GREEK LETTERS

α	phase volume fraction
ε	turbulent dissipation rate, m^2/s^3
δ_{li}	lower impeller inner edge thickness
δ_{lo}	lower impeller outer edge thickness
δ_u	upper impeller inner edge thickness
θ	particles temperature, K
θ_{li}	lower impeller inner edge bevel angle
θ_{lo}	lower impeller outer edge bevel angle
θ_u	upper impeller bevel angle
λ	phase dynamic viscosity, m^2/s
μ	phase dynamic viscosity, Pa·s
ρ	phase density, kg/m^3
τ	viscous stress tensor of phase
ψ	stitching function

SUBSCRIPTS AND SUPERSCRIPTS

av average
l liquid phase
li lower impeller inner edge
lo lower impeller outer edge
s solid phase
u upper impeller

REFERENCES

(1) Kafle, G. K.; Kim, S. H. Anaerobic Treatment of Apple Waste with Swine Manure for Biogas Production: Batch and Continuous Operation. *Appl. Energy* **2013**, *103*, 61−72.
(2) Bundhoo, M. A. Z.; Mohee, R. Inhibition of Dark Fermentative Bio-Hydrogen Production: A Review. *Int. J. Hydrogen Energy* **2016**, *41*, 6713.
(3) Gunyol, O.; Mudde, R. F. Computational Study of Hydrodynamics of a Standard Stirred Tank Reactor and a Large-Scale Multi-Impeller Fermenter. *Int. J. Multiscale Comput. Eng.* **2009**, *7*, 559−576.
(4) Yang, S.; Li, X.; Chao, Y.; Ma, B.; Mao, Z.-S. Computational Fluid Dynamics Simulation and Experimental Measurement of Gas and Solid Holdup Distributions in a Gas-Liquid-Solid Stirred Reactor. *Ind. Eng. Chem. Res.* **2016**, *55*, 3276.
(5) Wang, J.; Zhang, Y.; Wang, S.; Yang, C. Gas Dispersion and Solid Suspension in a Three-Phase Stirred Tank with Triple Impellers. *Chin. J. Chem. Eng.* **2019**, *28*, 1195.
(6) Tian, H.; Fotidis, I. A.; Mancini, E.; Angelidaki, I. Different cultivation methods to acclimatise ammonia-tolerant methanogenic consortia. *Bioresour. Technol.* **2017**, *232*, 1−9.
(7) Montante, G.; Magelli, F. Modelling of solids distribution in stirred tanks: analysis of simulation strategies and comparison with experimental data. *Int. J. Comput. Fluid Dyn.* **2005**, *19* (3), 253.
(8) Ashraf Ali, B.; B, K.; Madana, V. S. T. Experimental and computational investigation of solid suspension and gas dispersion in a stirred vessel. *Phys. Fluids* **2022**, *34* (11), 113318.
(9) Micheletti, M.; Nikiforaki, L.; Lee, K. C.; Yianneskis, M. Particle Concentration and Mixing Characteristics of Moderate-to-Dense Solid-Liquid Suspensions. *Ind. Eng. Chem. Res.* **2003**, *42*, 735−750.
(10) Li, G.; Gao, Z.; Li, Z.; Wang, J.; Derksen, J. J. Particle-Resolved PIV Experiments of Solid-Liquid Mixing in a Turbulent Stirred Tank. *AIChE J.* **2018**, *64* (9), 389.
(11) Blais, B.; Bertrand, O.; Fradette, L.; Bertrand, F. CFD-DEM Simulations of Early Turbulent Solid-Liquid Mixing: Prediction of Suspension Curve and Just-Suspended Speed. *Chem. Eng. Res. Des.* **2017**, *123*, 388−406.
(12) Hosseini, S.; Patel, D.; Ein-Mozaffari, F.; Mehrvar, M. Study of Solid-Liquid Mixing in Agitated Tanks through Computational Fluid Dynamics Modeling. *Ind. Eng. Chem. Res.* **2010**, *49* (4), 4426.
(13) Alberini, F.; Simmons, M. J. H.; Nienow, A. W.; Barigou, M. Angle-Resolved Particle Image Velocimetry Measurements of Flow and Turbulence Fields in Small-Scale Stirred Vessels of Different Mixer Configurations. *Ind. Eng. Chem. Res.* **2009**, *48* (2), 1034−1045.
(14) Bombač, A.; Zadravec, M.; Širok, B. Asymmetric Blade Disc Turbine for High Aeration Rates. *Stroj. Vestn./J. Mech.* **2018**, *64*, 513.
(15) Ameur, H.; Bouzit, M.; Bensakhria, A. Mixing of Complex Fluids in a Cylindrical Tank by a Modified Anchor Impeller. *ChemistrySelect* **2018**, *3* (42), 7472.
(16) Jamshidzadeh, M.; Ein-Mozaffari, F.; Lohi, A. Local and Overall Gas Holdup in an Aerated Coaxial Mixing System Containing a Non-Newtonian Fluid. *AIChE J.* **2021**, *66* (2), No. e17016.
(17) Steiros, K.; Bruce, P. J. K.; Buxton, O. R. H.; Vassilicos, J. C. Effect of Blade Modifications on the Torque and Flow Field of Radial Impellers in Stirred Tanks. *Phys. Rev. E: Stat. Phys., Plasmas, Fluids, Relat. Interdiscip. Top.* **2017**, *2* (9), 094802.
(18) Chen, Z.; Wu, Y.; Wang, J.; Luo, P. Study on the solid-liquid suspension behavior in a tank stirred by the long-short blades impeller. *Chin. J. Chem. Eng.* **2022**, *47* (7), 79−88.
(19) Zhang, W.; Gao, Z.; Yang, Q.; Zhou, S.; Xia, D. Study of Novel Punched-Bionic Impellers for High Efficiency and Homogeneity in PCM Mixing and Other Solid-Liquid Stirs. *Appl. Sci.* **2021**, *11* (21), 9883.
(20) Tamburini, A.; Brucato, A.; Busciglio, A.; Cipollina, A.; Grisafi, F.; Micale, G.; Scargiali, F.; Vella, G. Solid-Liquid Suspensions in Top-Covered Unbaffled Vessels: Influence of Particle Size, Liquid Viscosity, Impeller Size, and Clearance. *Ind. Eng. Chem. Res.* **2014**, *53* (23), 9587−9599.
(21) Zhou, S.; Yang, Q.; Lu, L.; Xia, D.; Zhang, W.; Yan, H. CFD Analysis of Sine Baffles on Flow Mixing and Power Consumption in Stirred Tank. *Appl. Sci.* **2022**, *12* (11), 5743.
(22) Hoseini, S. S.; Najafi, G.; Ghobadian, B.; Akbarzadeh, A. H. Impeller shape-optimization of stirred-tank reactor: CFD and fluid structure interaction analyses. *Chem. Eng. J.* **2021**, *413*, 127497.
(23) Yang, L.; Wang, J.; Sun, X.; Xu, M. Multi-objective optimization design of spiral demister with punched holes by combining response surface method and genetic algorithm. *Powder Technol.* **2019**, *355*, 106−118.
(24) Jin, W.; Mao, Z.; Zhou, S.; Zhang, T.; Hu, Y.; Wu, Z. Research on Multi-Optimal Project of Outlet Guide Vanes of Nuclear Grade Axial Flow Fan Based on Sensitivity Analysis. *Appl. Sci.* **2022**, *12*, 3029.
(25) Gidaspow, D. *Multiphase Flow and Fluidization: Continuum and Kinetic Theory Descriptions*; Academic Press: New York, 1994.
(26) Wang, S.; Jiang, X.; Wang, R.; Wang, X.; Yang, S.; Zhao, J.; Liu, Y. Numerical Simulation of Flow Behavior of Particles in a Liquid-Solid Stirred Vessel with Baffles. *Adv. Powder Technol.* **2017**, *28* (6), 1611−1624.
(27) Huilin, L.; Yurong, H.; Wentie, L.; Ding, J.; Gidaspow, D.; Bouillard, J. Computer simulations of gas-solid flow in spouted beds using kinetic-frictional stress model of granular flow. *Chem. Eng. Sci.* **2004**, *59* (4), 865−878.
(28) Tamburini, A.; Cipollina, A.; Micale, C.; Brucato, A.; Ciofalo, M. CFD simulations of dense solid-liquid suspensions in baffled stirred tanks: Prediction of solid particle distribution. *Chem. Eng. J.* **2012**, *223*, 875.
(29) Zwietering, T. N. Suspending of solid particles in liquid by agitators. *Chem. Eng. Sci.* **1958**, *8* (3−4), 244−253.
(30) Kraume, M. Mixing times in stirred suspensions. *Chem. Eng. Technol.* **1992**, *15* (5), 313−318.
(31) Ballester-Ripoll, R.; Paredes, E. G.; Pajarola, R. Sobol Tensor Trains for Global Sensitivity Analysis. *Reliab. Eng. Syst. Saf.* **2019**, *183*, 311−322.
(32) Xu, J.; Chen, Y.; Yan, H.; Yang, X. Optimizing Electromagnetic Cigarette Heaters Using PSO-NSGA II Algorithm: An Effective Strategy to Improve Temperature Control and Production Rate. *Appl. Artif. Intell.* **2023**, *37*, 2222257.
(33) Hörmann, T.; Suzzi, D.; Khinast, J. G. Mixing and Dissolution Processes of Pharmaceutical Bulk Materials in Stirred Tanks: Experimental and Numerical Investigations. *Ind. Eng. Chem. Res.* **2011**, *50* (21), 12104−12114.
(34) Kumaresan, T.; Nere, N. K.; Joshi, J. B. Effect of Internals on the Flow Pattern and Mixing in Stirred Tanks. *Ind. Eng. Chem. Res.* **2005**, *44* (26), 9951−9961.
(35) Yao, H.; Tang, Y.; Li, X.; Zhang, J.; Wang, J.; Wang, Y. Chaotic Mixing Intensification and Flow Field Evolution Mechanism in a Stirred Reactor Using a Dual-Shaft Eccentric Impeller. *Ind. Eng. Chem. Res.* **2022**, *61* (25), 9498.

https://doi.org/10.1021/acsomega.3c05762
ACS Omega 2023, 8, 47635−47645